Gliding motility of *Plasmodium* merozoites

Kazuhide Yahata[1,2,5,*], Melissa N. Hart[3,5], Heledd Davies[2], Masahito Asada[1,4], Thomas J. Templeton[1], Moritz Treeck[2], Robert W. Moon[3,*], Osamu Kaneko[1]

[1]Department of Protozoology, Institute of Tropical Medicine (NEKKEN), Nagasaki University, Nagasaki, Japan

[2]Signalling in Apicomplexan Parasites Laboratory, The Francis Crick Institute, London, UK

[3]Faculty of Infectious and Tropical Diseases, London School of Hygiene & Tropical Medicine, London, UK

[4]National Research Center for Protozoan Diseases, Obihiro University of Agriculture and Veterinary Medicine, Obihiro, Hokkaido, Japan

[5]These authors contributed equally

*Correspondence: kyahata@nagasaki-u.ac.jp or rob.moon@lshtm.ac.uk

Summary

Plasmodium malaria parasites use a unique form of locomotion termed gliding motility to move through host tissues and invade cells. The process is substrate-dependent and powered by an actomyosin motor that drives the posterior translocation of extracellular adhesins, which in turn propel the parasite forward. Gliding motility is essential for tissue translocation in the sporozoite and ookinete stages, however, the short-lived erythrocyte-invading merozoite stage has never been observed to undergo gliding movement. Here for the first time we reveal that blood stage *Plasmodium* merozoites use gliding motility for translocation in addition

to host cell invasion. We demonstrate that two human infective species, *P. falciparum* and *P. knowlesi*, have distinct merozoite motility profiles reflective of divergent invasion strategies. The process is powered by a conserved actomyosin motor and glideosome complex and is regulated by a complex signaling pathway. This significantly enhances our understanding of merozoite-host interactions in malaria parasites.

Keywords

Malaria, Merozoite, Erythrocyte invasion, Gliding motility

Introduction

Apicomplexan parasites traverse tissues and invade cells via a mechanism known as gliding motility, a unique process that uses neither propulsive structures such as flagella or cilia, nor cellular shape changes as for peristaltic and amoeboid motility (Russell et al., 1981; Dobrowolski et al., 1996). The system instead relies on the apical presentation of parasite transmembrane adhesins which bind to host substrates and then are drawn towards the parasite posterior by a conserved actomyosin motor running under the surface of the plasma membrane, resulting in the forward propulsion of the parasite (Tardieux et al., 2016; Frenal et al., 2017). Motility of invasive forms of malarial parasites (termed "zoites") was first described for the ookinete stage in avian blood (Danilewsky et al., 1889), and then for the sporozoite stage in the mosquito (Grassi et al., 1900). Unlike ookinetes and sporozoites, which must traverse through tissues, no gliding motility has been described for the merozoite, which invades erythrocytes in the bloodstream. Instead, only limited reorientation movement and cellular deformation has been observed across several malarial parasite species, including *Plasmodium knowlesi*, *P. falciparum,* and *P. yoelii* (Dvorak et al., 1975; Gilson et al., 2009; Yahata et al., 2012). Due to the short-lived nature and diminished size of merozoites (1–2 μm) relative to other zoites, it was presumed that merozoites do not require motility to encounter erythrocytes in the bloodstream, leading to the consensus that the molecular motor is principally required for penetration of the erythrocyte during invasion (Tardieux et al., 2016).

Here we show that both *P. falciparum* and *P. knowlesi* are capable of gliding motility across both erythrocyte surfaces and polymer coverslips, with distinctive dynamics between the two species. We have additionally developed a scalable

62 assay to evaluate the effect of genetic and pharmacological perturbations on both
63 the molecular motor and complex signaling cascade that regulates motility in
64 merozoites.
65

Results

Gliding motility of *Plasmodium* merozoites

Here we sought to address the long-standing question of whether malarial merozoites undergo conventional gliding motility. Whilst motility of sporozoites is normally observed on bovine serum albumin-coated glass slides, merozoites do not glide on this substrate. However, when using polymer coverslips with a hydrophilic coating (ibiTreat), we observed motile merozoites. When imaged immediately after erythrocyte egress, merozoites show directional movement on the coverslip surface which displaces them from the hemozoin containing residual body (Figure 1A, 1B and Movie S1, S2). *P. falciparum* merozoite gliding speed was 0.59 µm/second (n = 10), considerably slower than that of *Toxoplasma gondii* tachyzoites (helical gliding 2.60 µm/second, n = 13; circular gliding 1.84 µm/second, n = 13) and *Babesia bovis* merozoites (6.02 µm/second, n = 5). The longest gliding time of *P. falciparum* merozoites was 43 s, shorter than those of *T. gondii* tachyzoites (> 600 seconds) and *B. bovis* merozoites (125 seconds). The short-lived motility of *P. falciparum* merozoites correlates with the decline in erythrocyte invasion efficiency within a few minutes after egress (Boyle et al., 2010). The actin polymerization inhibitor cytochalasin D (10 µM) inhibited the directed movement of merozoites after egress from the erythrocyte, indicating the involvement of an actomyosin motor (Figure 1C and Movie S3).

The zoonotic malaria parasite, *P. knowlesi,* has much larger and longer-lived merozoites (Dennis et al., 1975), and thus we hypothesized that this may result in different gliding behavior. Advantageously, *P. knowlesi* merozoites are also less sensitive to light intensity than *P. falciparum.* We observed that freshly egressed *P. knowlesi* merozoites can glide across several human erythrocyte membranes prior to

invasion (Movie S4). *P. knowlesi* merozoites also exhibit some motility on ibiTreat coverslips, but the number of motile merozoites increases using poly-L-lysine-coated polymer coverslip surfaces (Movie S5), with on average 62% of merozoites within a given schizont exhibiting motility (Figure 2A). To confirm whether gliding is surface dependent, *P. knowlesi* merozoites were also monitored on uncoated polymer and glass coverslips. A much lower percentage of motile parasites was observed for the uncoated polymer (38%) and glass coverslips (25%) (Figure S1A). This suggests that both the coating and the use of polymer rather than glass coverslips is critical for optimal gliding to occur, and accounts for why merozoite motility has not been observed previously.

P. knowlesi was faster (1.06 μm/second, n = 57) than *P. falciparum* (Figure S1B) and was capable of gliding for up to 316 seconds (Figure 2B) on poly-L-lysine surfaces. Gliding was critical for post egress dispersal, as evidenced by the lack of dispersal of cytochalasin D-treated parasites (Figure 2A and Movie S6). Even without inhibitors merozoite movement was sometimes impaired by attachment to other parasites or the residual body. Merozoites often completed several glides, with a median cumulative distance of 14 μm, and some travelling as far as 200 μm within the 10-minute imaging window (Figure S1C). The majority of gliding occurred within 5 minutes of egress (Figure S1D), with peak gliding occurring during the initial 1-2 minute window. This time frame also correlates with invasion efficiency suggesting that, like for *P. falciparum*, motility could be used as a surrogate for invasive capacity. Gliding speed appeared to decline over subsequent glides (Figure S1E), indicative of declining motor function over time, which potentially contributes to the window of viability.

Like other *Plasmodium* zoites (Hakansson et al., 1999; Kudryashev et al., 2012; Asada et al., 2012), *P. knowlesi* merozoites appear to undergo corkscrew-like rotation (Movie S7), with a correlation between the number of turns and forward translocation, indicating a link between the two motions (Figure 2C and Figure 2D). On average, each body length the merozoite moved forward it rotated 0.8 times - equivalent to a tangential velocity of 61 μm/min, (n = 10). This is consistent with a linear motor running at a 42-degree angle down the longitudinal axis of the merozoite. Nine out of ten merozoites rotated counter-clockwise, demonstrating the same chirality seen for *Plasmodium* ookinetes (Kan et al., 2014). Rotation could not be discerned for *P. falciparum* merozoites, likely due to the round morphology and small size.

Interestingly, for both *Plasmodium* species, gliding and invasion proceeded with the wider end of the merozoite leading (Figure 2D) and not the narrower pointed end of the merozoite. The narrower pointed end has widely been suggested to contain the apical complex of the parasite, and indeed is consistent with early TEM images of invading parasites (Miller et al., 1979). To confirm that the apical complex is instead located within the wider end of the parasite we used live microscopy of AMA1-mNeonGreen tagged *P. knowlesi* parasites. This clearly shows that the apical end is located at the wider end of the zoite (Figure 2E and Movie S8), and that host cell entry proceeds in the same orientation as surface gliding, as has also been observed for *B. bovis* merozoites (Asada et al., 2012). Imaging of the AMA1-mNeonGreen parasite during invasion also shows, for the first time using live microscopy, the formation of a ring structure of the tight junction as the parasite invades the host erythrocyte (Figure 2E and Movie S8). A small protrusion likely corresponding to the apical complex is visible slightly offset from apex of the wider

front-end (Figure 2F, left hand image). It is the accentuation of this during the constriction of invasion depicted within classic electron microscopy images, which has likely led to the general assumption that merozoites uniformly narrow towards the apical end (Figure 2F). Whilst this is most clearly seen in the elongated forms of the *P. knowlesi* merozoites, it is also clear from videos of gliding in *P. falciparum* that the same holds true (Movie S2).

Gliding motility is powered by an actomyosin motor and glideosome complex

To determine the characteristics of the *P. falciparum* merozoite glideosome we evaluated the effect of chemical compounds and parasite genetic modifications on merozoite gliding motility. To overcome the light sensitivity of *P. falciparum* merozoites we developed an assay in which schizonts were seeded on coverslips in the dark at 37°C and incubated for 1 hour until the completion of merozoite egress. Motility could then be quantified by measuring the distance between a DAPI-stained merozoite nucleus and the hemozoin containing residual body (Figure 3A). The average merozoite-hemozoin distance measured for DMSO-treated merozoites (median 9.1 µm) was approximately equidistant to that observed for the time-lapse experiment (11.8 µm) and, as expected, the distance was significantly reduced by 0.1, 1 and 10 µM cytochalasin D treatment (7.1, 5.4 and 4.8 µm, respectively). Treatment with jasplakinolide, an actin filament stabilizer reported to increase the gliding speed of *T. gondii* tachyzoites, slightly but not significantly increased the distance, although it was not statistically significant (Figure 3B and S2).

We next examined conditional deletions of two essential glideosome components, actin-1 (ACT1) (Das et al., 2017) and glideosome-associated protein 45

(GAP45) (Perrin et al., 2018). Transgenic lines were able to egress after both the control DMSO treatment and upon rapamycin induced gene excision, but the merozoite–hemozoin distance was significantly reduced in the latter case (Figure 3C). When apical membrane antigen 1 (AMA1), a microneme protein important for erythrocyte attachment during invasion but unlikely to be involved in merozoite motility (Treeck, et al., 2009; Yang et al., 2017), was conditionally deleted, parasites were able to efficiently egress and motility assayed by the merozoite–hemozoin distance was not affected (Figure S3). These results confirm the involvement of the glideosome in *Plasmodium* merozoite gliding motility. During invasion, merozoite contact causes immediate erythrocyte membrane deformation before merozoite internalization (Gilson et al, 2009), however, the molecular basis of this phenomenon has not been elucidated. We found that rapamycin-treated ACT1- or GAP45-deleted parasites were not able to deform the erythrocyte (Figure 3D and 3E), in contrast to control DMSO-treated parasites or rapamycin-treated AMA1-deleted parasites (Figure S3). These results indicate that merozoite motility is required for erythrocyte deformation.

Gliding motility is regulated by a complex signaling pathway

Microorganelle discharge plays an essential role in the egress, gliding motility, and cell invasion of apicomplexan parasites and is regulated by a set of intracellular signaling enzymes, including calcium dependent protein kinases (Billker et al., 2009; Baker, 2017) phosphoinositide-phospholipase C (PI-PLC) (Singh et al., 2010), and diacylglycerol (DAG) kinase (Bullen et al, 2016). We evaluated whether these enzymes are also involved in the gliding motility of *P. falciparum* merozoites. Although the calcium ionophore A23187 (up to 100 µM) did not show a significant

effect, the calcium chelator BAPTA-AM (10 μM) significantly reduced merozoite–hemozoin distance ($p < 0.0001$; Figure 4A and S2). The PLC inhibitor U73122 (1 μM), but not the inactive analog U73343 (up to 10 μM), significantly reduced merozoite–hemozoin distance ($p < 0.0001$). The DAG kinase inhibitor R59022 (3 μM), which inhibits the conversion of DAG to phosphatidic acid (PA) also significantly reduced movement ($p < 0.001$), while the merozoite-hemozoin distance was not changed with propranolol, an inhibitor of phosphatidate phosphohydrolase (the converter of PA to DAG). Collectively, these results are consistent with reports on *Toxoplasma* tachyzoites (Bullen et al, 2016) and indicate that complex signaling pathways are involved in gliding motility of *P. falciparum* merozoites (Figure 4B).

Discussion

We show for the first time that *Plasmodium* merozoites possess gliding motility. We demonstrate merozoite gliding in two human infective species, *P. falciparum* and *P. knowlesi*. Motility could support a mechanism of cell sampling in the bloodstream, whereby the parasite moves across the surface of single or multiple erythrocytes until it is able to engage invasion receptors mediating successful invasion (McGhee, 1953). It is also plausible that the motility supports translocation and invasion in tissues such as the bone marrow, which is known to be a significant parasite reservoir for *P. vivax* (Obaldia et al., 2019). *P. knowlesi* merozoites glide nearly twice as fast and more than 7 times longer than *P. falciparum;* this difference likely underlies distinct invasion strategies. The potential for greater cellular sampling and prolonged interactions may therefore play a critical role in supporting invasion in less favorable conditions – potentially contributing to the relatively broad host range exhibited by this parasite. This may also prevent sub optimal receptor interactions by having gliding dominate until invasion competence is triggered by a threshold of erythrocyte receptors. In contrast, egress of *P. falciparum* merozoites occurs in the microvasculature of deep tissues where parasite-infected erythrocytes sequester with uninfected erythrocytes enabling merozoites to quickly encounter and invade new cells (Wahlgren et al., 2017). Cell sampling is therefore likely to be less important, and instead gliding may simply enhance erythrocyte receptor interactions.

Interestingly, this work has also enabled us to reverse our perception of the morphology of merozoites, with clear evidence from both gliding and fluorescently tagged parasites demonstrating that the apical complex actually resides in a small protrusion in the wider end of the zoite, rather than the pointy end of a tear shape as it is often depicted (Dasgupta et al., 2014). Whilst conceptually challenging, this is

exactly the same as is seen for *Plasmodium* ookinetes, which also lead with their wider end (Moon et al., 2009) and has important consequences for how we view and interpret images of invasion and understand the biophysical processes involved (Dasgupta et al., 2014).

Apicomplexan zoites utilize type 1 transmembrane proteins belonging to the TRAP family to adhere to environmental substrates for gliding. Two such proteins, merozoite thrombospondin-related anonymous protein (MTRAP) and thrombospondin-related apical membrane protein (TRAMP or PTRAMP), have been shown to be expressed at the merozoite stage (Boucher et al., 2015). MTRAP is dispensable for *P. falciparum* merozoites (Bargieri et al., 2016); however, transposon-based saturation mutagenesis analysis of *P. falciparum* suggested that TRAMP is essential for the blood stage parasite (Zhang et al., 2018), making it a prime candidate for future work to identify a merozoite gliding adhesin.

In conclusion, *Plasmodium* merozoites have the capacity for gliding motility, powered by a conserved actomyosin motor and glideosome complex, and controlled by a complex signaling cascade. The distinct gliding profiles of two different human infective species suggest divergent invasion strategies which provide new mechanisms to address questions of host selectivity and tissue reservoirs of the erythrocytic stages.

Acknowledgements

The authors thank Sujaan Das and Markus Meissner (supplying *P. falciparum* ACT1), Abigail Perrin and Michael Blackman (supplying *P. falciparum* GAP45:loxP), Alex Hunt (maintaining *T. gondii*). We also thank Reiko Tanaka, Nana Matsumoto, and Momoko Sakura for technical assistance. We are grateful to Japanese Red Cross Blood Society and UK NHS Blood and Transfusion Service for providing human erythrocyte and plasma. This study was conducted at the Joint Usage/Research Center on Tropical Disease, Institute of Tropical Medicine, Nagasaki University, Japan and London School of Hygiene and Tropical Medicine, UK. This work was supported by Fund for the Promotion of Joint International Research, Fostering Joint International Research, 16KK0183 (KY), 19KK0201 (KY), MEXT, Japan. This work was also supported in part by the Grants-in-Aids for Scientific Research, 15K08448 (KY), 19K07525 (KY), 16H05184 (OK), and 19H03461 (OK), MEXT, Japan. RWM was supported by a UK Medical Research Council Career Development Award (MR/M021157/1) and MNH was supported by a Bloomsbury Colleges Studentship. HD and MT receive funding from The Francis Crick Institute, which receives its core funding from Cancer Research UK (FC001189), the UK Medical Research Council (FC001189) and the Wellcome Trust (FC001189). The funders had no role in study design, data collection and analysis, decision to publish, or preparation of the manuscript.

Author Contributions

KY, MNH, RWM, MA, MT, and OK conceived and designed the experiments. KY and MNH performed experiments. HD helped with the generation of transgenic parasite

269 lines. KY, MNH, TT, MT, RWM and OK wrote the paper, and all authors contributed
270 to the manuscript and analyzed the data.

271

272 **Declaration of Interests**

273 The authors declare no competing interests.

Figure 1

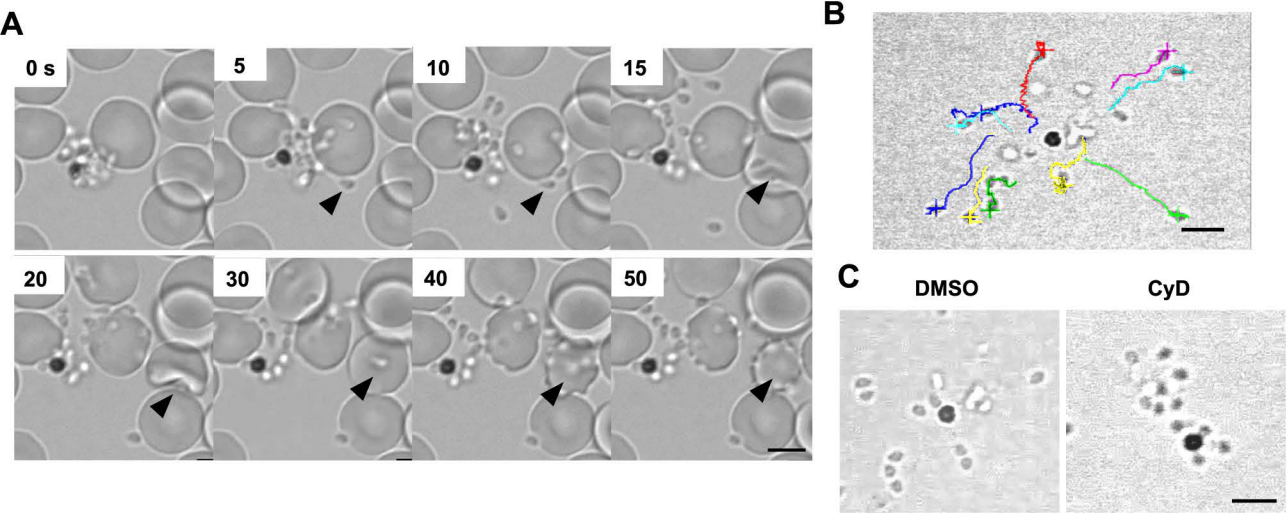

Figure 1. Gliding motility of *P. falciparum* merozoites. A, Time-lapse imaging for *P. falciparum* merozoite gliding motility and erythrocyte invasion. Still images from Movie S1. Arrowhead indicates a merozoite gliding on the coverslip (5 and 10 seconds), followed by erythrocyte deformation (15 and 20 seconds) and merozoite internalization (30–50 seconds). **B**, Each merozoite was traced in different colors and gliding speed was evaluated from Movie S2. **C**, Merozoite gliding motility was inhibited with 10 μM cytochalasin D (CyD, IC_{50} = 0.089 μM).

Figure 2

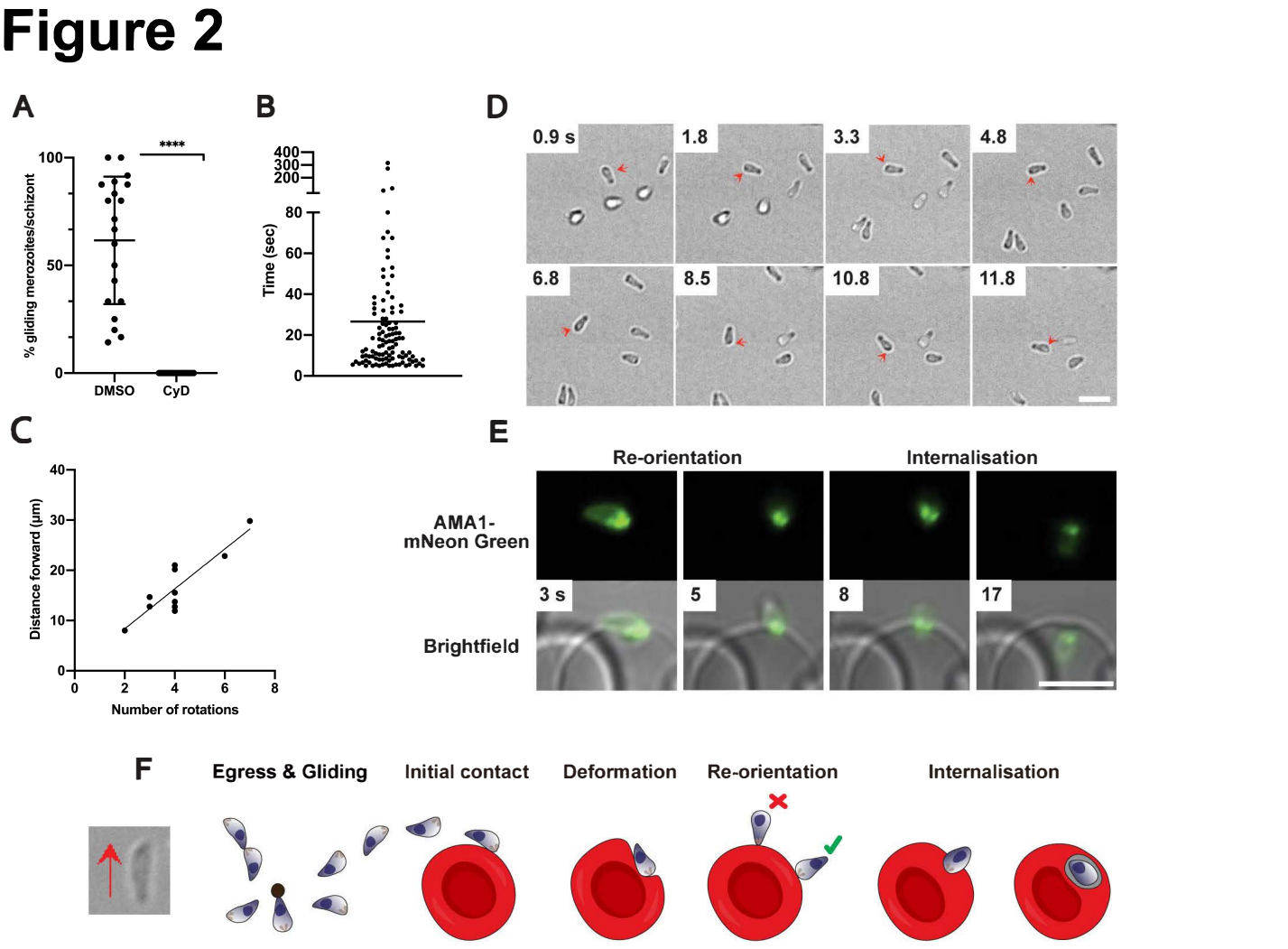
A
B
D
C
E
F
% gliding merozoites/schizont
****
DMSO
CyD
Time (sec)
0.9 s
1.8
3.3
4.8
6.8
8.5
10.8
11.8
Distance forward (µm)
Number of rotations
Re-orientation
Internalisation
AMA1-
mNeon Green
Brightfield
3 s
5
8
17
Egress & Gliding
Initial contact
Deformation
Re-orientation
Internalisation

298 **Figure 2. Gliding motility of *P. knowlesi* merozoites. A**, The percentage of
299 merozoites within a *P. knowlesi* schizont, which exhibit motility, both for DMSO-
300 treated parasites (mean = 62.5%) and CytoD-treated parasites (no gliding observed).
301 A 'motile' merozoite was defined as having demonstrated directional forward motion
302 along the surface of the coverslip for at least 5 continuous seconds. Each dot is
303 representative of one schizont (n = 20). Error bars denote +/- 1 s.d. **B**, The total time
304 each motile *P. knowlesi* merozoite (n= 109; median = 15 seconds) spent gliding
305 during the 10 minute imaging window post-egress. Error bars indicate interquartile
306 range. **C**, Number of rotations that merozoites completed plotted against the
307 distance travelled for each glide (n = 10). As the number of rotations increased, so
308 did the distance travelled forward, indicating rotation drives forward motion (Pearson
309 correlation coefficient, R = 0.88). **D**, Time lapse imaging demonstrating a *P. knowlesi*
310 merozoite rotating as it glides. Red arrows indicate a dark spot located to one side of
311 the wider end of the merozoite, which shifts to the opposite side (shown in
312 subsequent frames), as it turns, and then back to the original position to complete a
313 full rotation (see Movie S7). **E**, Time lapse imaging depicting an AMA1-mNeonGreen
314 tagged *P. knowlesi* merozoite invading an erythrocyte. Panels 1 and 2 demonstrate
315 re-orientation of the wide end of the merozoite to align with the erythrocyte
316 membrane. This is followed by the formation of the moving junction, depicted as two
317 green dots at the merozoite-erythrocyte interface (panel 3), and finally entry into the
318 host cell (panel 4). **F**, Schematic illustrating gliding and erythrocyte invasion. Gliding
319 proceeds with the wider, apical end of the merozoite leading. During gliding,
320 merozoites stretch, and a pointed protrusion can be seen at the wide end of the zoite
321 (left hand brightfield image), which engages with the erythrocyte membrane upon re-
322 orientation and internalisation. Re-orientation of the wider end (green tick), and not

the thinner, end of the zoite as previously hypothesized (red cross), occurs prior to entry. During internalisation, constriction of the apical end of the zoite causes the basal end to expand, causing static EM images to appear as if the wide end of the zoite is facing away from the erythrocyte. Finally, after entry is complete, the parasite resides in a parasitophorous vacuole where its development continues.

Figure 3

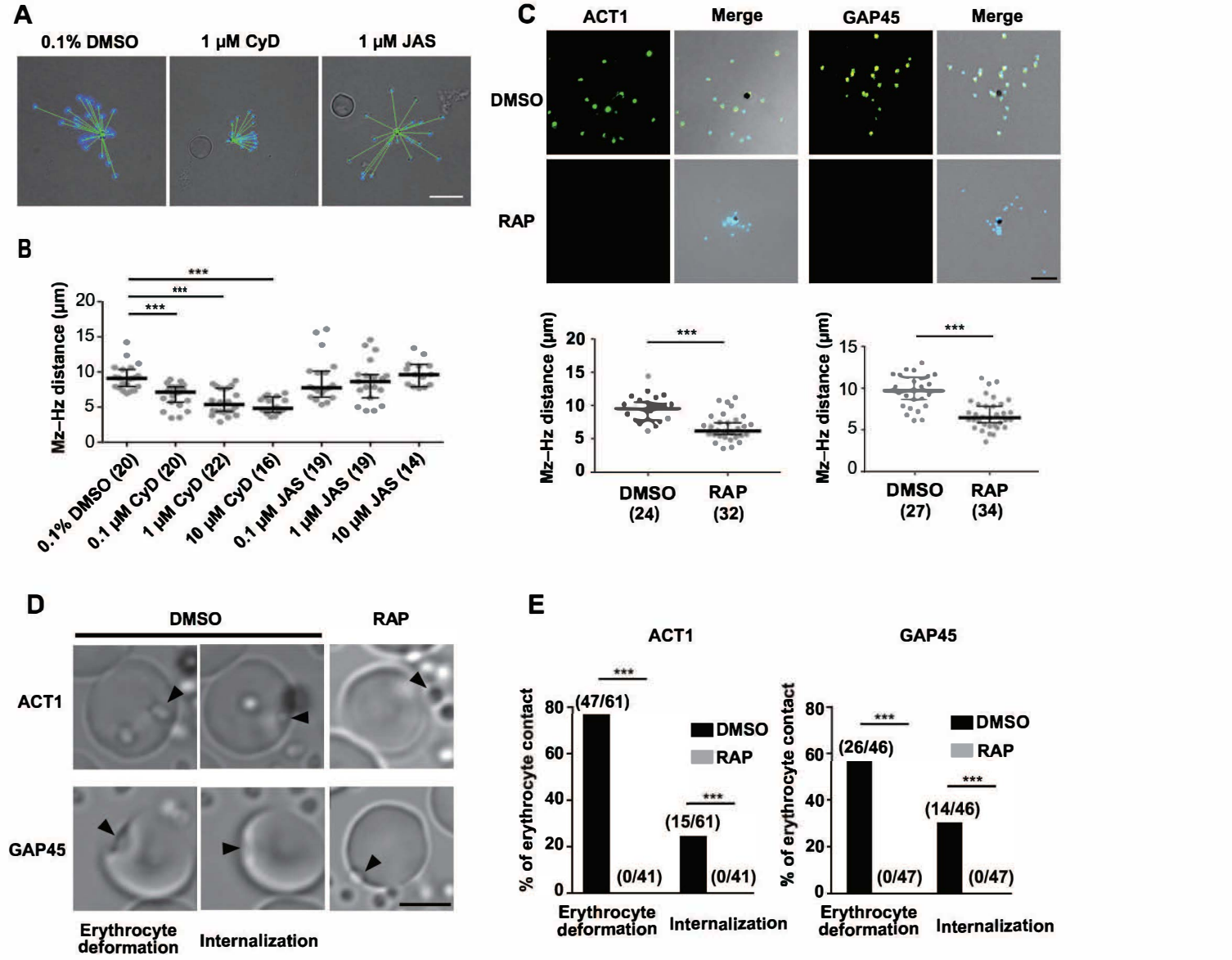
A
0.1% DMSO
1 µM CyD
1 µM JAS
B
Mz–Hz distance (µm)
0.1% DMSO (20)
0.1 µM CyD (20)
1 µM CyD (22)
10 µM CyD (16)
0.1 µM JAS (19)
1 µM JAS (19)
10 µM JAS (14)
C
ACT1
Merge
GAP45
Merge
DMSO
RAP
Mz–Hz distance (µm)
DMSO (24)
RAP (32)
DMSO (27)
RAP (34)
D
DMSO
RAP
ACT1
GAP45
Erythrocyte deformation
Internalization
E
ACT1
GAP45
% of erythrocyte contact
DMSO
RAP
(47/61)
(0/41)
(15/61)
(0/41)
(26/46)
(0/47)
(14/46)
(0/47)
Erythrocyte deformation
Internalization

Figure 3. The effect of chemical compounds and parasite genetic modifications on *P. falciparum* merozoite gliding motility. Purified *P. falciparum* schizonts were seeded on the coverslip and merozoite egress was allowed. **A**, The distance of the merozoite nucleus (DAPI, Mz) from hemozoin (black pigment, Hz) was measured (green line, Mz–Hz distance). Where indicated in the y-axes (panels **B**, **C**, **E**) the Mz–Hz distance obtained from each schizont with their median and interquartile range are shown. The number of analyzed schizonts from two biological replicates are indicated in the parentheses. **B**, Effect of 0.1% DMSO, 0.1, 1, or 10 μM cytochalasin D (CyD), or jasplakinolide (JAS, IC_{50} = 0.085 μM) were evaluated for merozoite gliding motility. *** indicates $p < 0.0001$. **C**, Inhibition of gliding motility in rapamycin (RAP)-treated ACT1- or GAP45-deleted *P. falciparum* parasites. IFA with specific antibodies indicated ACT1 or GAP45 were not detected in RAP-treated transgenic parasites. *** indicates $p < 0.0001$ by the Mann-Whitney test. **D**, **E**, Erythrocyte deformation and merozoite internalization events were seen for DMSO-treated parasites, but not detected after RAP-treatment ($p < 0.001$ for all by two-tailed Fisher's exact test). Scale bar represents 5 μm.

Figure 4

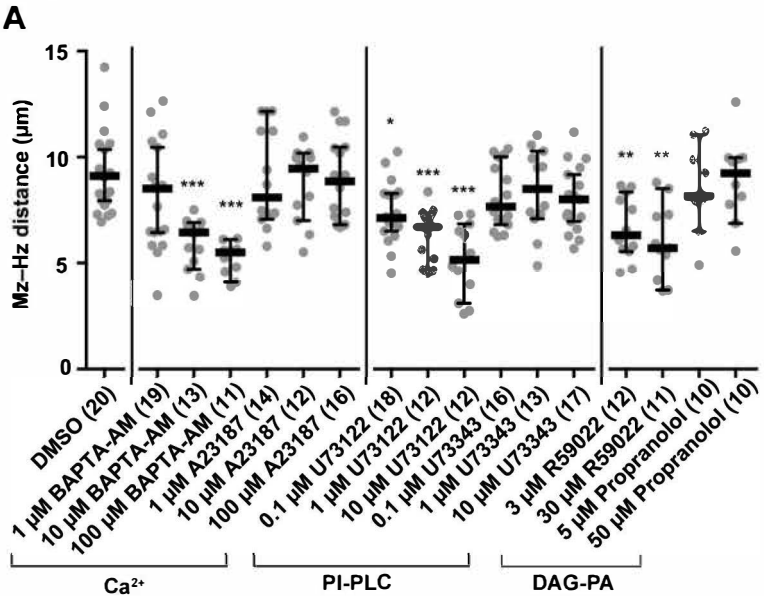
A
Mz–Hz distance (µm)
15
10
5
0
*
***
***
*
***
***
**
**
DMSO (20)
1 µM BAPTA-AM (19)
10 µM BAPTA-AM (13)
100 µM BAPTA-AM (11)
1 µM A23187 (14)
10 µM A23187 (12)
100 µM A23187 (16)
0.1 µM U73122 (18)
1 µM U73122 (12)
10 µM U73122 (12)
0.1 µM U73343 (16)
1 µM U73343 (13)
10 µM U73343 (17)
3 µM R59022 (12)
30 µM R59022 (11)
5 µM Propranolol (10)
50 µM Propranolol (10)
Ca2+
PI-PLC
DAG-PA

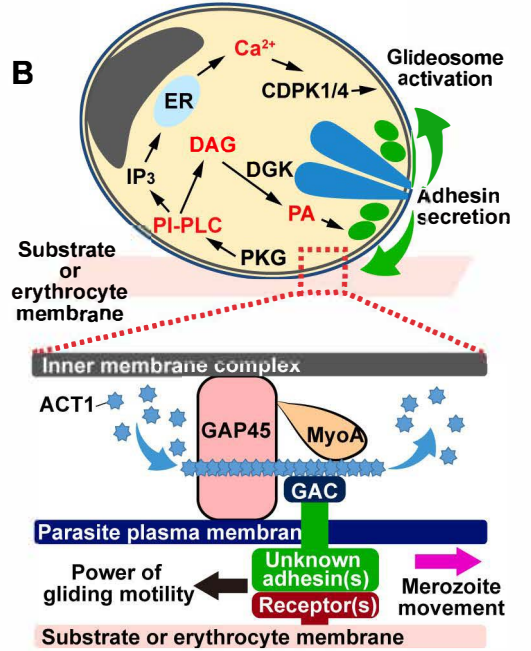
B
Ca2+
Glideosome activation
ER
CDPK1/4
DAG
DGK
IP3
PA
PI-PLC
PKG
Adhesin secretion
Substrate or erythrocyte membrane
Inner membrane complex
ACT1
GAP45
MyoA
GAC
Parasite plasma membrane
Power of gliding motility
Unknown adhesin(s)
Receptor(s)
Merozoite movement
Substrate or erythrocyte membrane

Figure 4. Signaling pathways involved in gliding motility of *P. falciparum* merozoite. A, Purified *P. falciparum* schizonts were treated with BAPTA-AM (IC_{50} = 1.54 µM), A23187 (IC_{50} = 0.89 µM), U73122 (IC_{50} = 0.33 µM), U73343 (IC_{50} = 2.39 µM), R59022 (IC_{50} = 4.77 µM), or propranolol (IC_{50} = 3.75 µM) and merozoite gliding assays were performed. *, **, ***, and **** indicate $p < 0.05$, < 0.01, 0.001, and < 0.0001, respectively. **B**, Overview of molecular mechanisms for gliding motility of *P. falciparum* merozoite. After merozoite egress from the erythrocyte, merozoite adhesin(s) are secreted from micronemes (green) via a signaling pathway involving phosphoinositide-phospholipase (PI-PLC) and diacylglycerol (DAG) kinase (DGK) and bind to environmental substrates including the erythrocyte membrane. A pathway involving PI-PLC and Ca^{2+} activates calcium dependent protein kinases (CDPKs) and phosphorylates the components of the glideosome machinery (Billker et al, 2009; Singh et al, 2010; Bullen et al., 2016; Baker, 2017; Fang et al., 2018). Grey, nucleus and blue, rhoptries. Gliding motility is powered by an actomyosin motor of the glideosome machinery and the merozoite movement is transferred to the erythrocyte membrane causing erythrocyte deformation upon merozoite attachment. ACT1, actin-1; IMC, inner membrane complex; PKG, cyclic GMP-dependent protein kinase; PA, phosphatidic acid; GAP45, glideosome-associated protein 45; MyoA, myosin-A; and GAC, glideosome-associated connector.

Methods

Parasite culture and transfection

P. falciparum Dd2 parasites were maintained with O^+ human erythrocytes in RPMI1640 medium (Invitrogen) supplemented with 25 mM HEPES (Sigma), 0.225% sodium bicarbonate (Invitrogen), 0.1 mM hypoxanthine (Sigma), 25 µg/mL

gentamicin (Invitrogen), 0.5% AlbuMax I (Invitrogen), essentially as described[28]. The ACT1 (Das et al., 2017), GAP45:loxP (Perrin et al., 2018), and AMA1:loxP *P. falciparum* lines (Tibúrcio et al., 2019) were cultured with A^+ human erythrocytes. WR99210 and G418 were used to generate ACT1 and AMA1:loxP parasite lines, respectively. The *T. gondii* RH strain was cultured in a confluent monolayer of human foreskin fibroblasts (HFFs) maintained in Dulbecco's Modified Eagle Medium (DMEM), GlutaMAX supplemented with 10% fetal bovine serum, at 37°C and 5% CO_2. The *B. bovis* Texas strain was maintained in purified bovine erythrocytes with GIT medium (WAKO, Osaka, Japan) at 37°C with a microaerophilic stationary-phase culture system. A1-H.1 *P. knowlesi* parasites were maintained in human erythrocytes (UK National Blood Transfusion Service) with custom made RPMI-1640 medium, supplemented with 10% Horse Serum (v/v) and 2 mM L-glutamine according to previously described methods (Moon et al., 2013). Mature schizonts were purified by gradient centrifugation on a 55% Nycodenz layer (Progen, Heidelberg, Germany), as described (Moon et al., 2013). Tightly synchronized schizonts were transfected using the Amaxa 4-D electroporator and P3 Primary Cell 4D Nucleofector X Kit L (Lonza) according to the protocol described by Moon et al. (2013).

Generation of *P. knowlesi* AMA-1 mNeonGreen tagged parasites

P. knowlesi AMA-1 mNeonGreen tagged parasites were generated by insertion of an mNeonGreen (mNG) sequence immediately before the *AMA1* stop codon (Figure S2A) using the CRISPR Cas9 system described by Mohring et al., 2019 (sgRNA

sequence: GAGAAGCCTTACTACTGAGT). Donor DNA was synthesized by overlapping PCR, as previously described for PkAMA-1-HA tagged parasites (Mohring et al., 2019) and included the mNeonGreen sequence flanked by 500 bp sequences homologous to the c-terminal (HR1) and 3'UTR (HR2) regions of the AMA-1 locus (Figure S2A). Primers for PCR listed in Table S1. In brief, HR1 and HR2 were both PCR amplified from *P. knowlesi* A1 H1 gDNA (with primers P6/P7 and P8/P9 respectively), while the mNeonGreen sequence was amplified from Plasmid Pk_mNeonGreen with primers P10/P11. All three fragments were subsequently assembled together in two successive steps: firstly by fusing fragments HR1 and mNeonGreen (primers P12/P13), and secondly by fusing fragments HR1/mNeonGreen and HR2 (primers P12/P15) to create the final product, HR1/mNeonGreen/HR2. Post transfection, integration of donor DNA was confirmed by diagnostic PCR, using primers P1 and P3 (Figure S2B). Expression of the AMA-1-mNG fusion protein was also confirmed by indirect immunofluorescence assay (Figure S2C). Air-dried smears of late stage schizonts were fixed in 4% PFA for half an hour and permeabilised with 0.1% Triton-X100 for 10 mins. Slides were subsequently blocked in 3% BSA overnight, before labelling with mouse anti-mNeonGreen [32F6] (1:300, Chromotek) followed by goat Alexa Fluor 488 anti-mouse (1:1000, Invitrogen). Nuclei were stained with ProLong Gold Antifade Mountant (Invitrogen). Images were collected using an inverted microscope (Ti-E; Nikon, Japan) with a 60x oil objective lens (N.A. 1.4).

443 **Inducible gene-knockout *P. falciparum* parasites**

444 The *GAP45*, *Act1*, and *AMA1* genes were excised by rapamycin treatment from
445 GAP45:loxP, ACT1, and AMA1:loxP *P. falciparum* parasites, respectively (Jones et
446 al., 2016). Briefly, ring stage parasites synchronized by 5% sorbitol method were
447 treated with 100 nM rapamycin (Sigma, St. Louis, USA) or 0.1% DMSO for 12 hours.
448 Schizonts were purified with a 5D magnet separation column (MACS, Miltenyi
449 Biotech, Germany) and used for gliding or erythrocyte invasion assays.

450

451 **Time lapse imaging for the gliding motility of *P. falciparum* merozoites, *P.***
452 ***knowlesi* merozoites, *T. gondii* tachyzoites, and *B. bovis* merozoites**

453 Time lapse imaging assays for *P. falciparum* merozoites were performed at 37ºC
454 using an inverted microscope (Ti-E; Nikon, Japan) with a 60x oil objective lens (N.A.
455 1.4 or 1.47). *P. falciparum* synchronized schizonts in incomplete medium without
456 AlbuMAX I were transferred to the ibiTreat µ-Slide $I^{0.4}$ Luer channel slide (Ibidi,
457 Germany) and incubated for 10 minutes at 37ºC to allow the parasite-infected
458 erythrocytes to attach to the bottom. Incomplete medium was removed and replaced
459 with complete RPMI medium prewarmed to 37ºC, then parasites were observed by
460 microscopy. Likewise, synchronized *P. knowlesi* schizonts were transferred using the
461 same technique to either ibiTreat, poly-L-lysine-coated, uncoated, or glass µ-Slide
462 $I^{0.4/0.5}$ Luer channel slides (Ibidi) in incomplete RPMI medium and incubated at 37ºC
463 for 10 minutes to allow cell attachment. Subsequently, incomplete medium was
464 replaced with complete RPMI medium with 10% horse serum, as per normal
465 culturing conditions. For the actin inhibitor treatments, *P. falciparum* and *P. knowlesi*
466 schizonts were allowed to attach to coverslips while suspended in incomplete RPMI

467 medium, which was then replaced with their respective complete RPMI medium
468 additionally containing 0.1–10 μM cytochalasin D (Sigma) or 0.1% DMSO (Sigma). *T.*
469 *gondii* tachyzoites growing in HFFs were collected by scraping after the culture
470 medium was replaced with ENDO buffer (Endo et al., 1987). Intracellular parasites
471 were isolated from HFFs by lysing host cells via passaging 20 times through a
472 syringe and tachyzoites were transferred to an ibiTreat μ-Slide $I^{0.4}$ Luer channel slide
473 and incubated for 15 minutes at 37ºC. The slide was placed on the microscope stage,
474 and the medium was replaced with DMEM before observation. *B. bovis* parasites
475 were isolated in RPMI medium then transferred to the ibiTreat μ-Slide $I^{0.4}$ Luer
476 channel slide. All parasites were observed by differential interference contrast or
477 bright field at 1.5V/100W of halogen lamp or LED light (pT-100; CoolLED, UK) to
478 minimize cell damage. Time-lapse images were captured at 1–100 frames per
479 second using a digital camera (ORCA-R2 or ORCA-Flash4.0; Hamamatsu photonics,
480 Shizuoka, Japan) and imaged using the NIS-Element Advanced Research imaging
481 software (Nikon). Gliding speed was calculated either manually using distance
482 measurement tools or by the tracking module within the NIS-Element software
483 (Nikon). The tangential speed of *P. knowlesi* merozoites was determined by
484 calculating the number of rotations/minute and multiplying this value by the average
485 circumference of a merozoite. The angle of the motor was subsequently calculated
486 using the formula Tan(x) = R/L, where x = the angle of the motor, R = the average
487 distance each merozoite rotated/per body length travelled forward, and L = the body
488 length of the merozoite.

489

490

491

492 **_P. falciparum_ merozoite gliding assay**

493 *P. falciparum* schizonts were purified with a 5D magnet separation column, then
494 adjusted to 1 x 10^5 cell/ml with incomplete RPMI medium and loaded onto an ibiTreat
495 µ-Slide $VI^{0.4}$ chamber slide (ibidi). The chamber slides were incubated for 10 min at
496 17°C to allow schizont attachment to the bottom followed by replacing the medium
497 with complete RPMI medium containing chemical compounds or DMSO control.
498 Slides were incubated at 17°C for 1 hour then the temperature was increased to
499 37°C for 1 hour to allow parasite egress. Parasites were fixed with 1%
500 paraformaldehyde fixation solution, which was then replaced with PBS containing
501 3% BSA (Sigma) and 100 ng/ml DAPI (Invitrogen). For the indirect
502 immunofluorescence assay, parasites were fixed in 4% paraformaldehyde containing
503 0.0075% glutaraldehyde (Nacalai Tesque, Japan) and permeabilized with PBS
504 containing 0.1% Triton-X100 (Calbiochem, CA, USA), then blocked with PBS
505 containing 3% BSA. Next, samples were immunostained with mouse anti-*P.*
506 *falciparum* ACT1 (final dilution 1:500; a kind gift from Jake Baum) or rat anti-HA
507 (1:1000, Roche) for HA-tagged GAP45 and AMA1. This was followed by 3 × washes
508 with PBS then incubation with Alexa Fluor 488 goat anti-mouse or Alexa Fluor 594
509 goat anti-rat antibodies (1:1000; Invitrogen) in PBS containing 3% BSA with DAPI
510 (Invitrogen). Stained parasites were mounted with Prolong Gold antifade reagent
511 (Invitrogen). Microscopy images (Ti-E, Nikon) of egressed merozoites were cropped
512 to 47 x 47 μm^2 to measure the distance of merozoite nuclei (stained with DAPI) from
513 hemozoin in the residual body (malaria pigment, with bright field image) using NIS-
514 Elements software (Nikon). Statistical analysis was performed by the Kruskal-Wallis

515 test followed by Dunn's multiple comparison test using PRISM 6 software (GraphPad
516 Software, Inc., CA, USA).

517

518 **Chemical Compounds**

519 Complete RPMI medium was supplemented with cytochalasin D, jasplakinolide
520 (Sigma), 1,2-Bis(2-aminophenoxy)ethane-N,N,N',N'-tetraacetic acid
521 tetraacetoxymethyl ester (BAPTA-AM, Invitrogen, CA, USA), calcium Ionophore
522 A23187 (Sigma), U73122 (Calbiochem), U73343 (Calbiochem), R59022 (Tocris
523 bioscience, UK), propranolol (Sigma), or DMSO. Compound concentrations were as
524 described (Singh et al, 2010; Bullen et al., 2016). IC_{50} values for *P. falciparum* were
525 determined using a protocol available at WorldWide Antimalarial Resistance Network
526 (WWARN-
527 http://www.wwarn.org/sites/default/files/INV08_PFalciparumDrugSensitivity.pdf).

528

Reference

Asada, M., Goto, Y., Yahata, K., Yokoyama, N., Kawai, S., Inoue, N., Kaneko, O., and Kawazu, S. (2012). Gliding motility of *Babesia bovis* merozoites visualized by time-lapse video microscopy. PLoS One *7*, e35227.

Baker, D.A., Drought, L.G., Flueck, C., Nofal, S.D., Patel, A., Penzo, M., and Walker, E.M. (2017). Cyclic nucleotide signalling in malaria parasites. Open Biol. *7*(12).

Bargieri, D.Y., Thiberge, S., Tay, C.L., Carey, A.F., Rantz, A., Hischen, F., Lorthiois, A., Straschil, U., Singh, P., Singh, S. et al. (2016) Plasmodium merozoite TRAP family protein is essential for vacuole membrane disruption and gamete egress from erythrocytes. Cell Host Microbe *20*, 618-630.

Billker, O., Lourido, S. and Sibley, L. D. (2009). Calcium-dependent signaling and kinases in apicomplexan parasites. Cell Host Microbe *5*, 612–622.

Boucher, L. E. and Bosch, J. (2015) The apicomplexan glideosome and adhesins — structures and function. J. Struct. Biol. *190*, 93–114.

Boyle, M. J., Wilson, D.W., Richards, J.S., Riglar, D.T., Tetteh, K.K., Conway, D.J., Ralph, S.A., Baum, J., and Beeson, J.G. (2010). Isolation of viable *Plasmodium falciparum* merozoites to define erythrocyte invasion events and advance vaccine and drug development. Proc. Natl. Acad. Sci. U. S. A. *107*, 14378–14383.

Bullen, H. E., Jia, Y., Yamaryo-Botté, Y., Bisio, H., Zhang, O., Jemelin, N. K., Marq, J. B., Carruthers, V., Botté, C. Y., & Soldati-Favre, D. (2016). Phosphatidic Acid-mediated signaling regulates microneme secretion in Toxoplasma. Cell Host Microbe *19*, 349–360.

Danilewsky, B. (1889). La Parasitologie Comparée du Sang. Kharkoff.

552 Das, S., Lemgruber, L., Tay, C. L., Baum, J. & Meissner, M. (2017). Multiple
553 essential functions of *Plasmodium falciparum* actin-1 during malaria blood-stage
554 development. BMC Biol. *15*, 70.
555 Dasgupta, S., Auth, T., Gov, N.S., Satchwell, T.J., Hanssen, E., Zuccala, E.S., Riglar,
556 D.T., Toye, A.M., Betz, T., Baum, J., et al. (2014). Membrane-wrapping contributions
557 to malaria parasite invasion of the human erythrocyte. Biophys. J. *107*, 43-54.
558 Dennis, E.D., Mitchell, G.H., Butcher, G.A., and Cohen, S. (1975). In vitro isolation of
559 *Plasmodium knowlesi* merozoites using polycarbonate sieves. Parasitology *71*, 475–
560 481.
561 Dobrowolski, J.M., and Sibley, L.D. (1996). Toxoplasma invasion of mammalian cells
562 is powered by the actin cytoskeleton of the parasite. Cell *84*, 933-939.
563 Dvorak, J.A., Miller, L.H., Whitehouse, W.C., and Shiroishi, T. (1975). Invasion of
564 erythrocytes by malaria merozoites. Science *187*, 748–750.
565 Endo, T., Tokuda, H., Yagita, K., and Koyama, T. (1987). Effects of extracellular
566 potassium on acid release and motility initiation in *Toxoplasma gondii*. J. Protozool.
567 *34*, 291–295.
568 Fang, H., Klages, N., Pino, P., Maco, B., Brochet, M., Gomes, A.R., Zenonos, Z.A.,
569 Walker, E.M., Baker, D.A., Angrisano, F., et al. (2018). Epistasis studies reveal
570 redundancy among calcium-dependent protein kinases in motility and invasion of
571 malaria parasites. Nat. Commun. *9*, 4248
572 Frenal, K., Dubremetz, J. F., Lebrun, M. and Soldati-Favre, D. (2017). Gliding motility
573 powers invasion and egress in Apicomplexa. Nature Rev. *15*, 645–660.
574 Gilson, P. R. and Crabb, B. S. (2009). Morphology and kinetics of the three distinct
575 phases of red blood cell invasion by *Plasmodium falciparum* merozoites. Int. J.
576 Parasitol. *39*, 91–6.

577 Grassi, B. Studi di uno zoologo sulla malaria. (1900). R. Accademia dei Lincei.

578 Hakansson, S., Morisaki, H., Heuser, J. and Sibley, L. D. (1999). Time-lapse video
579 microscopy of gliding motility in *Toxoplasma gondii* reveals a novel, biphasic
580 mechanism of cell locomotion. Mol. Biol. Cell. *10*, 3539–47.

581 Jones, M.L., Das, S., Belda, H., Collins, C.R., Blackman, M.J., and Treeck, M. (2016).
582 A versatile strategy for rapid conditional genome engineering using loxP sites in a
583 small synthetic intron in *Plasmodium falciparum*. Sci. Rep. *6*, 2180.

584 Kan, A., Tan, Y.H., Angrisano, F., Hanssen, E., Rogers, K.L., Whitehead, L., Mollard,
585 V.P., Cozijnsen, A., Delves, M.J., Crawford, S., et al. (2014). Quantitative analysis of
586 *Plasmodium* ookinete motion in three dimensions suggests a critical role for cell
587 shape in the biomechanics of malaria parasite gliding motility. Cell. Microbiol. *5*,
588 734-50.

589 Kudryashev, M., Münter, S., Lemgruber, L., Montagna, G., Stahlberg, H.,
590 Matuschewski, K., Meissner, M., Cyrklaff, M., and Frischknecht, F. (2012). Structural
591 basis for chirality and directional motility of Plasmodium sporozoites. Cell. Microbiol.
592 *14*, 1757–68.

593 McGhee, R. B. (1953). The infection by *Plasmodium lophurae* of duck erythrocytes in
594 the chicken embryo. J. Exp. Med. *97*, 773–82.

595 Miller, L.H., Aikawa, M., Johnson, J.G., and Shiroishi, T. (1979). Interaction between
596 cytochalasin B-treated malarial parasites and erythrocytes: Attachment and junction
597 formation. J. Exp. Med. *149*, 172-84.

598 Mohring, F., Hart, M.N., Rawlinson, T.A., Henrici, R., Charleston, J.A., Diez
599 Benavente, E., Patel, A., Hall, J., Almond, N., Campino, S., et al. (2019). Rapid and
600 iterative genome editing in the malaria parasite *Plasmodium knowlesi* provides new
601 tools for *P. vivax* research. Elife. *8*, e45829.

602 Moon, R.W., Taylor, C.J., Bex, C., Schepers, R., Goulding, D., Janse, C.J., Waters,
603 A.P., Baker, D.A., and Billker, O. (2009). A cyclic GMP signalling module that
604 regulates gliding motility in a malaria parasite. PLoS Pathog. *9*, e1000599.
605 Moon, R.W., Hall, J., Rangkuti, F., Ho, Y.S., Almond, N., Mitchell, G.H., Pain, A.,
606 Holder, A.A., and Blackman, M.J. (2013). Adaptation of the genetically tractable
607 malaria pathogen *Plasmodium knowlesi* to continuous culture in human erythrocytes.
608 Proc. Natl. Acad. Sci. U. S. A. *110*, 531–536.
609 Obaldia, N., Meibalan, E., Sa, J.M., Ma, S., Clark, M.A., Mejia, P., Moraes Barros,
610 R.R., Otero, W., Ferreira, M.U., Mitchell, J.R., et al. (2018). Bone marrow is a major
611 parasite reservoir in *Plasmodium vivax* infection. MBio *9,* e00625-18.
612 Perrin, A.J., Collins, C.R., Russell, M.R.G., Collinson, L.M., Baker, D.A., and
613 Blackman, M.J. (2018). The actinomyosin motor drives malaria parasite red blood
614 cell invasion but not egress. MBio *9*, e00905-18.
615 Russell D. G. and Sinden R. E. (1981). The role of the cytoskeleton in the motility of
616 coccidian sporozoites. J. Cell. Sci*. 50*: 345-59.
617 Singh, S., Alam, M. M., Pal-Bhowmick, I., Brzostowski, J. A. and Chitnis, C. E.
618 (2010). Distinct external signals trigger sequential release of apical organelles during
619 erythrocyte invasion by malaria parasites. PLoS Pathog. *6*, e1000746.
620 Tardieux, I., and Baum, J. (2016). Reassessing the mechanics of parasite motility
621 and host-cell invasion. J. Cell. Biol. *214*, 507–515.
622 Tibúrcio, M., Yang, A.S.P., Yahata, K., Suárez-Cortés, P., Belda, H., Baumgarten, S.,
623 van de Vegte-Bolmer, M., van Gemert, G.-J., van Waardenburg, Y., Levashina, E.A.,
624 et al. (2019). A novel tool for the generation of conditional knockouts to study gene
625 function across the *Plasmodium falciparum* life cycle. MBio *10.* e01170-19.

626 Trager, W. and Jensen, J. B. (1976). Human malaria parasites in continuous culture.
627 Science *193*, 673–675.
628 Treeck, M., Zacherl, S., Herrmann, S., Cabrera, A., Kono, M., Struck, N.S.,
629 Engelberg, K., Haase, S., Frischknecht, F., Miura, K., et al. (2009). Functional
630 analysis of the leading malaria vaccine candidate AMA-1 reveals an essential role for
631 the cytoplasmic domain in the invasion process. PLoS Pathog. *5*, e1000322.
632 Wahlgren, M., Goel, S. and Akhouri, R. R. (2017). Variant surface antigens of
633 *Plasmodium falciparum* and their roles in severe malaria. Nat. Rev. Microbiol. 15,
634 479–491.
635 Yahata, K., Treeck, M., Culleton, R., Gilberger, T. W. and Kaneko, O. (2012). Time-
636 lapse imaging of red blood cell invasion by the rodent malaria parasite *Plasmodium*
637 *yoelii*. PLOS ONE *7,* e50780.
638 Yang, A.S.P., and Boddey, J.A. (2017). Molecular mechanisms of host cell traversal
639 by malaria sporozoites. Int. J. Parasitol. *47*, 129-136.
640 Zhang, M., Wang, C., Otto, T.D., Oberstaller, J., Liao, X., Adapa, S.R., Udenze, K.,
641 Bronner, I.F., Casandra, D., Mayho, M., et al. (2018). Uncovering the essential
642 genes of the human malaria parasite *Plasmodium falciparum* by saturation
643 mutagenesis. Science *360,* eaap7847.
644

Supplemental Information

Gliding motility of *Plasmodium* merozoites

Kazuhide Yahata[1,2,5,*], Melissa N. Hart[3,5], Heledd Davies[2], Masahito Asada[1,4], Thomas J. Templeton[1], Moritz Treeck[2], Robert W. Moon[3,*], Osamu Kaneko[1]

Supplementary Figures

Figure S1. *P. knowlesi* merozoite gliding speed and duration.

Figure S2. Generation of *P. knowlesi* AMA-1 mNeonGreen tagged parasites.

Figure S3. *P. falciparum* merozoite gliding assay with a panel of chemical compounds.

Figure S4. Effect of AMA1-deletion for merozoite gliding motility, erythrocyte deformation, and merozoite internalization.

Supplementary Movies

Movie S1: *P. falciparum* merozoite gliding motility and erythrocyte invasion. Parasites were imaged on an ibiTreat coverslip at a rate of 100 frames/second.

Movie S2: Gliding motility of *P. falciparum* merozoites with DMSO. Parasites treated with 0.1% DMSO were imaged on an ibiTreat coverslip at a rate of 100 frames/second.

Movie S3: Gliding motility of *P. falciparum* merozoites with cytochalasin D (CyD). Parasites treated with 10 µM CyD were imaged on an ibiTreat coverslip at a rate of 10 frames/second.

Movie S4: Live microscopy of *P. knowlesi* merozoites completing several short glides on the surface of erythrocytes. Parasites were imaged on a poly-L-lysine-coated coverslip at a rate of 1 frame/second. A red arrow appears at the beginning of each glide.

Movie S5: *P. knowlesi* merozoites treated with 0.005% DMSO gliding on the surface of a poly-L-lysine-coated coverslip. Parasites were filmed immediately post egress at a rate of 1 frame/second.

Movie S6: Egress of *P. knowlesi* merozoites treated with 100 nM CyD on the surface of a poly-L-lysine-coated coverslip. Parasites were filmed at a rate of 1 frame/second.

Movie S7: *P. knowlesi* merozoite, designated by a red cross, demonstrating corkscrew-like rotation, while travelling across a poly-L-lysine-coated coverslip. Parasites were filmed at a rate of 10 frames/second.

Movie S8: AMA1-mNeonGreen tagged *P. knowlesi* merozoite invading an erythrocyte via its 'wide' apical end. Parasites were filmed at a rate of 1 frame/second.

Supplementary Table

Table S1: Primers for PCR listed for generation of *P. knowlesi* AMA-1 mNeonGreen tagged parasites.

Supplementary Figures

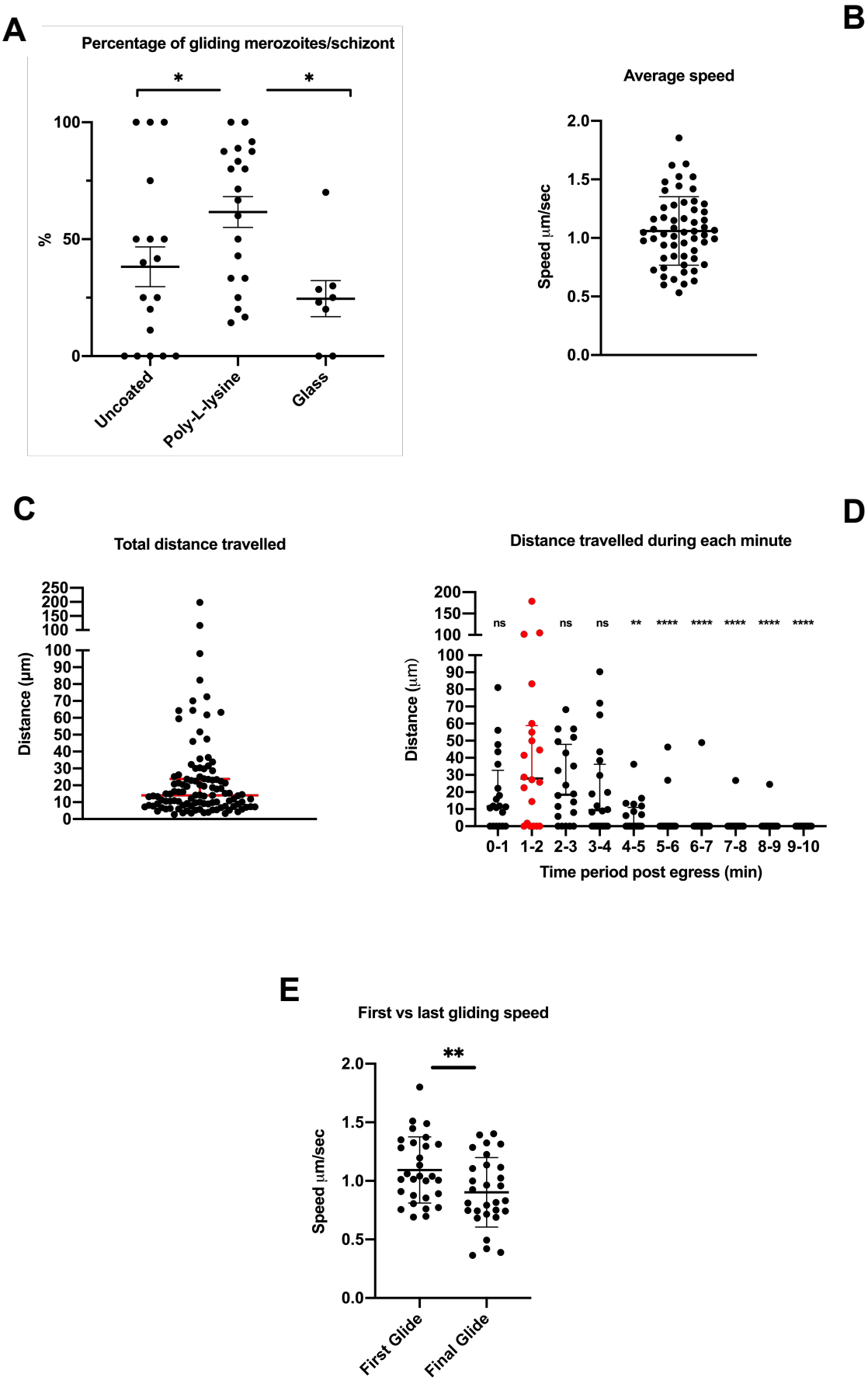

Figure S1: *P. knowlesi* merozoite gliding speed and duration. A, merozoite motility on different surfaces. The percentage of merozoites exhibiting motility decreases from 62% on poly-L-lysine surfaces (n = 20 schizonts) to 38% on uncoated surfaces (n = 18 schizonts; * $p < 0.05$) and 25% on glass surfaces (n = 8; * $p < 0.02$). Means compared using one-way ANOVA and Dunnett's multiple comparison test**.** Error bars denote +/- 1 s.d. **B,** Speeds of individual merozoites (average = 1.06 µm/second; n = 57 merozoites). Error bars denote +/- 1 s.d. **C**, Total distance travelled by each merozoite. Merozoites travelled a median distance of 14 µm during the 10-minute window of imaging (minimum = 2.8 µm, maximum = 198.6 µm; n = 109 merozoites). **D**, Distances travelled by schizonts (a total of distances travelled by each merozoite) during each minute post egress (n = 20 schizonts). The majority of gliding occurred within 5 minutes post egress, with peak gliding (median of 28 µm travelled) occurring 1-2 minutes post egress (** $p < 0.01$, **** $p < 0.0001$, as determined by a Kruskal-Wallis test). This delay is likely due to a small 'settling period' during the first 60 seconds, while merozoites disperse and begin to connect to the slide coverslip. Error bars denote interquartile range. **E**, First vs last gliding speeds. Comparison by two-tailed paired t-test between the speed of the first and final glides of merozoites (* $p < 0.005$; n = 29) shows that gliding speed decreases from 1.09 µm/second (average first glide) to 0.90 µm/second (average last glide), indicative of decreasing gliding efficiency over time. Error bars denote +/- 1 s.d.

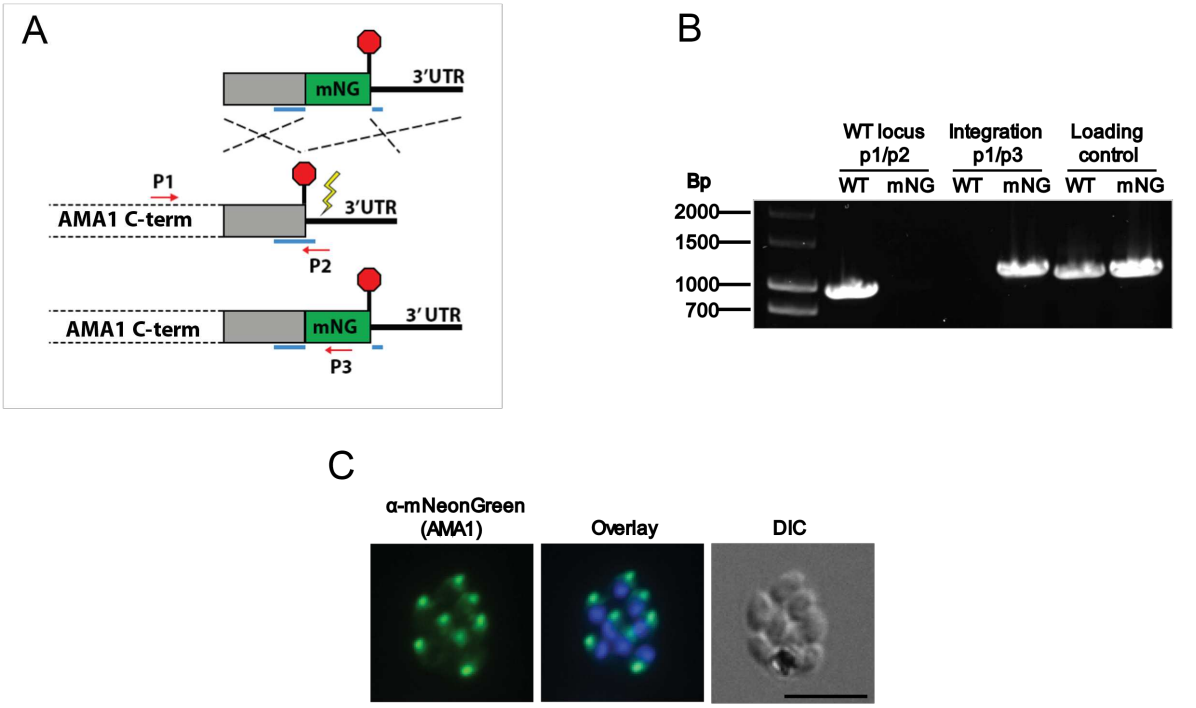

Figure S2: Generation of *P. knowlesi* AMA-1 mNeonGreen tagged parasites. A, Schematic depicting integration of mNeonGreen tagging construct into the *AMA1* locus. Donor DNA was synthesized by overlapping PCR, and consisted of the mNG sequence flanked by 500 bp homology regions to the c-terminus and 3'UTR regions of the Pk*AMA1* locus. A sgRNA (position underlined in blue) targeted a CRISPR Cas9 induced double stranded break (yellow lightning) immediately after the stop codon. Upon repair, the target sequence was split in two by the insertion of the tag, ablating further Cas9 activity. Positions of diagnostic primers indicated by red arrows. **B**, Diagnostic PCR showing the absence of WT parasites (primers P1/P2; expected band size 988 bp), and the presence of transgenic parasites (primers P1/P3; expected band size 1118 bp) in transfected line, along with control PCR reaction detecting unrelated locus. Primers for PCR listed in Table S1.**C**, Indirect immunofluorescence assay detecting the AMA1-mNeonGreen fusion protein. Antibody specific for the mNeonGreen tag detects protein expressed in late stage schizonts, localized to the apical poles of merozoites. Scale bar indicates 5 μm.

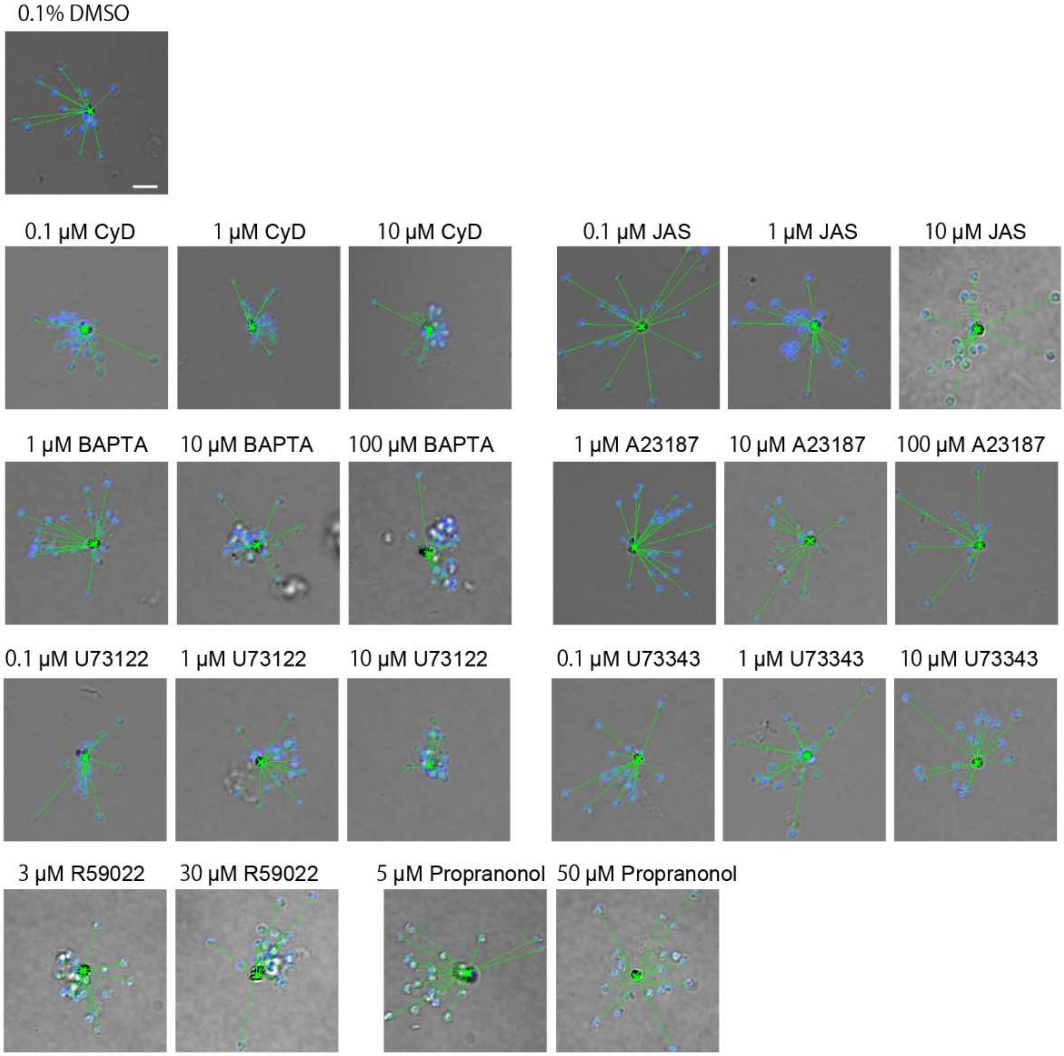

Figure S3: *P. falciparum* merozoite gliding assay with a panel of chemical compounds. Compound-treated merozoites were allowed to egress and fixed. The distance between merozoite DNA stained with Hoechst33342 (Blue) and hemozoin were measured (green line). Cytochalasin D (CyD), jasplakinolide (JAS), BAPTA-AM (BAPTA), A23187, U73122, U73343, R59022, and propranolol were used in this assay. Scale bar represents 5 µm.

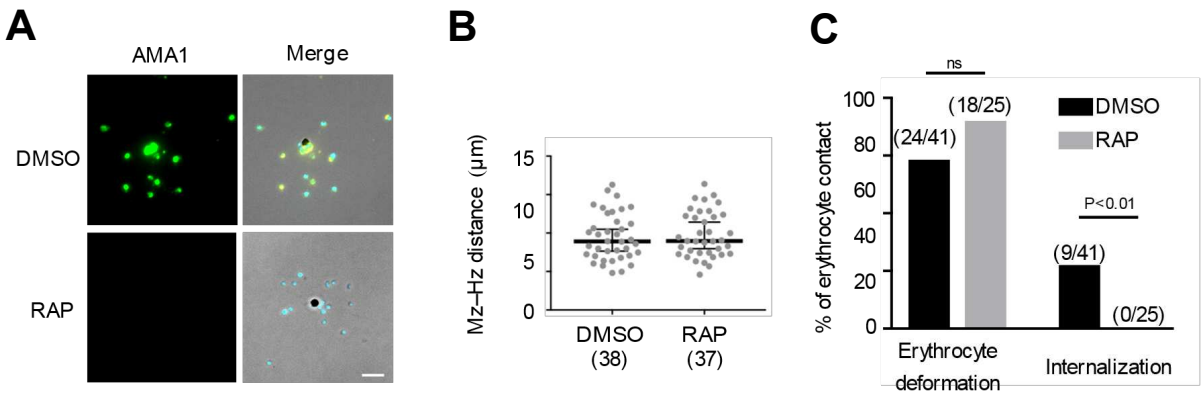

Figure S4: Effect of AMA1-deletion for merozoite gliding motility, erythrocyte deformation, and merozoite internalization. **A**, PfAMA1:loxP parasite line was treated with DMSO or rapamycin (RAP) and merozoites egressed from infected erythrocytes were stained with anti-AMA1 antibody (green). Right panels, merged images of green AMA1 signals, blue nucleus signals, and differential interference contrast images. **B**, The merozoite (Mz)-hemozoin (Hz) distances (median and interquartile range) were obtained from two biological replicates. No statistically significant difference was detected between DMSO- and RAP-treated parasites by two-tailed Fisher's exact test. **C**, The number of erythrocyte deformation events was not different between DMSO- and RAP-treated parasites. However, merozoite internalization events seen for DMSO-treated parasites were not detected in RAP-treated AMA1-deleted parasites ($p < 0.01$ by two-tailed Fisher's exact test). ns, not significant. Scale bar represents 5 μm.